Asian Journal of Atmospheric Environment
Vol. 11, No. 4, pp. 270-282, December 2017
doi: https://doi.org/10.5572/ajae.2017.11.4.270
ISSN (Online) 2287-1160, ISSN (Print) 1976-6912

Numerical Simulations of Dry and Wet Deposition over Simplified Terrains

T. Michioka[1),2),*], H. Takimoto[1)], H. Ono[1)] and A. Sato[1)]

[1)]Environmental Science Research Laboratory, Central Research Institute of Electric Power Industry, 1646 Abiko, Abiko-shi, Chiba-ken 270-1194, Japan
[2)]Department of Mechanical Engineering, Kindai University, 3-4-1 Kowakae, Higashiosaka, Osaka, 577-8502, Japan

*Corresponding author. Tel: +81-6-4307-3475, E-mail: michioka@mech.kindai.ac.jp

ABSTRACT

To evaluate the deposition amount on a ground surface, mesoscale numerical models coupled with atmospheric chemistry are widely used for larger horizontal domains ranging from a few to several hundreds of kilometers; however, these models are rarely applied to high-resolution simulations. In this study, the performance of a dry and wet deposition model is investigated to estimate the amount of deposition via computational fluid dynamics (CFD) models with high grid resolution. Reynolds-averaged Navier-Stokes (RANS) simulations are implemented for a cone and a two-dimensional ridge to estimate the dry deposition rate, and a constant deposition velocity is used to obtain the dry deposition flux. The results show that the dry deposition rate of RANS generally corresponds to that observed in wind-tunnel experiments. For the wet deposition model, the transport equation of a new scalar concentration scavenged by rain droplets is developed and used instead of the scalar concentration scavenged by raindrops falling to the ground surface just below the scavenging point, which is normally used in mesoscale numerical models. A sensitivity analysis of the proposed wet deposition procedure is implemented. The result indicates the applicability of RANS for high-resolution grids considering the effect of terrains on the wet deposition.

Key words: Atmospheric dispersion, Dry deposition, High-grid resolution, Numerical simulation, Wet deposition

1. INTRODUCTION

Wet and dry deposition on ground surfaces is very important for predicting the concentration of aerosol particles, pollutants, sea salt particles, and radioactive materials emitted from various sources (e.g., plants, automobiles, and seas) in the atmosphere. To evaluate the deposition amount, mesoscale numerical models coupled with atmospheric chemistry have widely been used for larger horizontal domains ranging from a few to several hundreds of kilometers (Morino *et al*., 2015; Terada and Chino, 2008). However, deposition areas on local scales are not resolved in mesoscale numerical models due to the low grid resolution.

Parker and Kinnersley (2004) investigated the effect of complex topography on the dry deposition rate in a wind-tunnel experiment and showed that it strongly affects the pattern of dry deposition. Pesava *et al*. (1999) investigated the dry deposition rate of particles to building (cube) surfaces in a wind-tunnel experiment and reported that the deposition velocity averaged over a cube side was nearly ten times higher than that on a flat surface. Janhäll (2015) reviewed the effect of urban vegetation on pollutant dispersion and deposition and reported that urban vegetation affects air quality by influencing pollutant dispersion and deposition. To estimate the exact deposition area, a high-resolution numerical simulation considering complex terrain, buildings, and vegetation is required. Michioka and Chow (2008) implemented a high-resolution large-eddy simulation (LES) model with a horizontal grid resolution of 25 m to simulate gas dispersion over a complex terrain. They showed that the LES model applied in a mesoscale setting has the ability to predict gas dispersion at high grid resolutions. Michioka *et al*. (2013) also implemented a high-resolution LES model coupled to a mesoscale LES model for gas dispersion to estimate a 1-hour average ground concentration in an urban area. Nakayama *et al*. (2015) implemented an LES-based CFD model with a mesoscale model to simulate turbulent winds with buoyancy effects under actual meteorological conditions. Kondo *et al*. (2006) investigated boundary conditions for the Reynolds-averaged Navier–Stokes (RANS) model to reproduce the dispersion of NO_x around the

Ikegami-Shinmachi crossroads in Tokyo and suggested that the calculations with the boundary conditions from the mesoscale model were more accurate. Hendricks *et al.* (2007) evaluated the RANS model (RUSTIC, for Realistic Urban Spread and Transport of Intrusive Contaminants) coupled with a Lagrangian particle transport and diffusion model (MESO). The inflow velocity profiles were given by a minisodar, and the ground concentration obtained by the RANS was compared with an observation in the central business district of Oklahoma City. They concluded that meteorological inputs are the most important factors for predicting the ground concentration. Therefore, high-resolution CFD models have been applied to predict gas concentrations; however, there are only a few studies of dry and wet deposition in a local area.

The most frequently used formulation for dry deposition assumes that the flux is proportional to the concentration of the depositing species at some reference height above the surface (Seinfeld and Pandis, 2006). The proportionality constant between the flux and the concentration is usually called the deposition velocity, which is often given as a constant value (Terada *et al.*, 2004). The process of dry deposition is generally represented as consisting of three processes: aerodynamic transport, molecular or Brownian transport, and uptake at the surface. The deposition velocity is also estimated by a resistance model that incorporates the aerodynamic resistance, quasi-laminar sublayer resistance, and surface resistance (Wesely, 1989; Slinn and Slinn, 1980). The reference concentration for the dry deposition model is usually used as the first grid concentration above the surface, and this height is tens of meters above the surface in a mesoscale model but only a few meters in a high-resolution CFD model. Therefore, the applicability of the frequently used formulation for dry deposition to a high-resolution CFD model must be investigated.

With regard to wet deposition, the fluxes of gases and particles into rain droplets below a cloud is approximately proportional to the concentration. The proportionality constants between the flux and the concentration are known as the scavenging coefficients (Seinfeld and Pandis, 2006), and a scalar scavenged by a raindrop immediately falls to the ground surface (Kajino *et al.*, 2012). This assumption is reasonable for a mesoscale numerical simulation using structured grids because the horizontal grid resolution is normally several kilometers. However, for a high-resolution numerical simulation using an unstructured grid, this assumption is not exactly valid. For example, under high wind conditions, a scalar scavenged by a raindrop at several meters above the surface is dispersed in the horizontal direction by the wind before moving to the surface and the scalar is deposited to the ground surface grid, which is different from the grid directly below the scavenging point. High-resolution numerical simulations for the Fukushima nuclear accident using grids of 1 km or less have been implemented by Katata *et al.* (2012a, b) and Sekiyama *et al.* (2015); however, they assumed that the scalar scavenged by the hydrometeors (rain, snow, and graupel) immediately reached the ground surface. Even though the increasing availability of powerful computers makes more high-resolution numerical simulations feasible, a wet deposition model for mesoscale simulations has not yet been developed. In addition, when an unstructured grid is used, it is not easy to find the surface grids related to those at the scavenging points due to the programming complexity. Therefore, for high-resolution numerical simulations using unstructured grids, the frequently used model cannot estimate the wet deposition rate at an exact position.

To implement a high-resolution numerical simulation for dry and wet deposition using an unstructured grid, the applicability of the dry deposition model needs to be investigated and a new wet deposition model needs to be developed. In this study, a RANS simulation using a fine grid resolution is implemented for a cone and a two-dimensional ridge to estimate the dry deposition rate and the results are compared to wind-tunnel experiments (Parker and Kinnersley, 2004). For the wet deposition model, the transport equation of a new scalar concentration scavenged by rain droplets is developed and a sensitivity analysis of the proposed wet deposition procedure is implemented.

2. NUMERICAL SIMULATION

The continuity, momentum, and mass conservation equations can be written as

$$\frac{\partial U_i}{\partial x_i} = 0, \tag{1}$$

$$\frac{\partial U_i}{\partial t} + \frac{\partial U_j U_i}{\partial x_j} = -\frac{1}{\rho}\frac{\partial P}{\partial x_i} + \frac{\partial}{\partial x_j}\left[(\nu + \nu_T)\left(\frac{\partial U_i}{\partial x_j} + \frac{\partial U_j}{\partial x_i}\right)\right], \tag{2}$$

$$\frac{\partial C}{\partial t} + \frac{\partial U_j C}{\partial x_j} = \frac{\partial}{\partial x_j}\left[\left(D + \frac{\nu_T}{Sc_t}\right)\frac{\partial C}{\partial x_j}\right] + S_q - W_d - F, \tag{3}$$

where U_i is the velocity component, C is the gas concentration, P is the pressure, ρ is the density, ν ($= 1.5 \times 10^{-5}$ m^2/s) is the kinematic viscosity of air, D ($= 1.5 \times 10^{-5}$ m^2/s) is the molecular diffusion coefficient, ν_T is the eddy viscosity, W_d is the wet deposition flux, F is the dry deposition flux, and S_q is the source

term of the tracer gas. The turbulent Schmidt number (Sc_t) is set to 0.7 (Tominaga and Stathopoulos, 2007).

The governing equations (Eqs. (1)-(3)) are solved directly using the Front Flow/Red (FFR) code (Michioka *et al*., 2013; Kurose *et al*., 2012) extended by CRIEPI (Central Research Institute of Electric Power Industry) and NuFD (Numerical Flow Designing, Ltd), which are solved via the finite volume method with an unstructured grid. In Eq. (2), the eddy viscosity is modeled using the RNG k-ε model:

$$\nu_t = C_\mu \frac{k^2}{\varepsilon}, \tag{4}$$

where k and ε are the turbulent kinetic energy and its dissipation rate, respectively, which can be written as

$$\frac{\partial k}{\partial t} + \frac{\partial U_j k}{\partial x_j} = \frac{\partial}{\partial x_j}\left[\left(\nu + \frac{\nu_T}{\sigma_k}\right)\frac{\partial k}{\partial x_j}\right] + P_k - \varepsilon, \tag{5}$$

$$\frac{\partial \varepsilon}{\partial t} + \frac{\partial U_j \varepsilon}{\partial x_j} = (C^*_{\varepsilon 1} P_k - C_{\varepsilon 2}\varepsilon)\frac{\varepsilon}{k} + \frac{\partial}{\partial x_j}\left[\left(\nu + \frac{\nu_T}{\sigma_\varepsilon}\right)\frac{\partial \varepsilon}{\partial x_j}\right], \tag{6}$$

$$C^*_{\varepsilon 1} = C_{\varepsilon 1} - \frac{\eta\left(1 - \frac{\eta}{\eta_0}\right)}{1 + \beta\eta^3}, \tag{7}$$

$$\eta = \frac{k}{\varepsilon}\sqrt{2S_{ij}S_{ij}}, \text{ and} \tag{8}$$

$$S_{ij} = \frac{1}{2}\left(\frac{\partial U_i}{\partial x_j} + \frac{\partial U_j}{\partial x_i}\right). \tag{9}$$

The model constants have the following default values: $\sigma_k = \sigma_\varepsilon = 1/1.39$, $C_{\varepsilon 1} = 1.42$, $C_{\varepsilon 2} = 1.68$, $C_\mu = 0.085$, $\eta_0 = 0.085$, and $\beta = 0.012$.

The dry deposition flux F near the surface is proportional to the concentration of the species,

$$F = -v_d C_1, \tag{10}$$

where v_d is the deposition velocity and C_1 is the concentration at the lowest grid points near the surface. Equation (10) is valid in the grids adjacent to the surface and in other grids with $F = 0$. The wet deposition flux is normally modeled by the following equation,

$$W_d = \Lambda C, \tag{11}$$

where Λ is the scavenging coefficient. The wet deposition flux is generally valid in the presence of clouds, rain, and snow; however, only rainwater is considered in the presented simulations. Following Seinfeld and Pandis (2006), the cloud-scavenging rate F_c is

$$F_c = \int_0^h \Lambda(z,t)\, C(x,y,z,t)\, dz, \tag{12}$$

where h is the cloud base height. This assumption is reasonable for mesoscale numerical simulations using structured grids because the horizontal grid resolution is normally several kilometers. However, for a high-resolution numerical simulation using an unstructured grid, which is often used, this assumption is not exactly valid.

To estimate the exact wet deposition fluxes, the transport equation of a new scalar Y, which is the concentration scavenged by rain, is solved in this study:

$$\frac{\partial Y}{\partial t} + \frac{\partial U_j Y}{\partial x_j} + W_j \frac{\partial Y}{\partial x_j} = \frac{\partial}{\partial x_j}\left[\left(D + \frac{\nu_T}{Sc_t}\right)\frac{\partial Y}{\partial x_j}\right] + W_d, \tag{13}$$

where W is the terminal velocity of the raindrop. The transport equation of rainwater R is

$$\frac{\partial R}{\partial t} + \frac{\partial U_j R}{\partial x_j} + W_j \frac{\partial R}{\partial x_j} = \frac{\partial}{\partial x_j}\left[\left(D + \frac{\nu_T}{Sc_t}\right)\frac{\partial R}{\partial x_j}\right] + S_R, \tag{14}$$

where S_R is the formation rate of the raindrop, which can be inferred from the precipitation intensity. Microphysics, such as the evaporation of rain and the accretion of rain by cloud ice and graupel, should be added to Eq. (14) (Lin *et al*., 1983). However, they are not considered in this simulation because the microphysics processes are very complicated and the purpose of this simulation is not to exactly solve the equation of the raindrop but to investigate the applicability of the transport equation of the proposed scalar concentration scavenged by rain droplets.

3. COMPARISON OF WIND-TUNNEL DATA FOR DRY DEPOSITION

Parker and Kinnersley (2004) conducted wind-tunnel experiments for dry deposition to understand the pattern of small particles over a landscape. In this study, the flow and deposition fields predicted by the presented RANS are validated against the wind-tunnel experiments.

3.1 Computational Conditions

Fig. 1 shows a schematic diagram of the computational domains for the two-dimensional hill and cone. The computational domains are 4.4 m × 1.0 m × 1.7 m in the $x \times y \times z$ dimensions. Two simplified terrain models, which are used in the wind-tunnel experiment by Parker and Kinnersley (2004), are applied in the presented RANS. The first terrain model is a two-dimensional hill with a height of 0.1 m ($=H_1$) and a lateral width of 1.0 m, which is equal to the lateral length of the computational domain, and the flat side ridges have slopes of 45°. The top of the ridge is located at 1.4 m ($=14H_1$) downwind of the inlet boundary

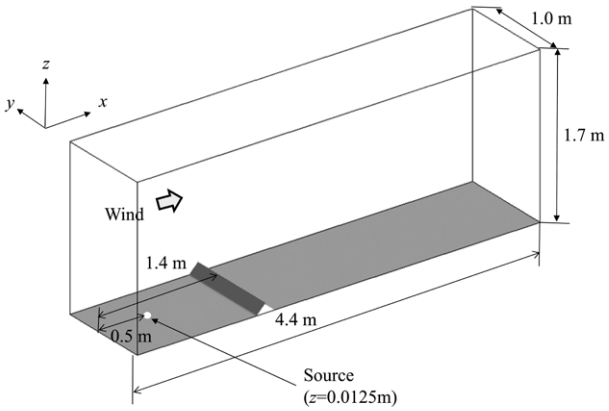

(a) Two-dimensional hill

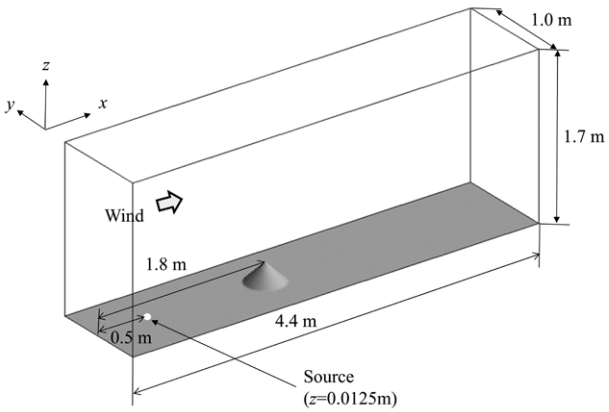

(b) Cone

Fig. 1. The computational domains for dry deposition.

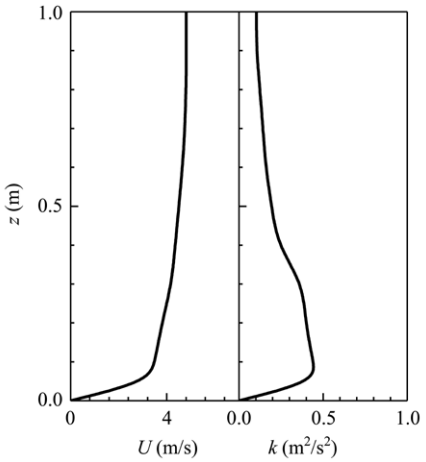

Fig. 2. The inflow conditions for the velocity and turbulent kinetic energy.

and 3.0 m ($=30H_1$) upwind of the outlet boundary. The three-dimensional terrain is conical in shape and has a height of 0.2 m ($=H_2$) with a slope of 45°. The conical point is located at 1.8 m ($=9H_2$) downwind of the entrance and 2.6 m ($=13H_2$) upwind of the outlet boundary. The distance between the conical point and the sidewalls is 0.5 m ($=2.5H_2$), which is smaller than the recommended distance of $5.0H_2$ in COST Action 732 (Franke *et al.*, 2007). However, in COST Action 732, the recommended value is suggested due to a wind-tunnel experiment and CFDs for a single block or an urban area with multiple buildings, which is different from the cone in this simulation. The accuracy of the presented RANS is confirmed by a wind-tunnel experiment by Parker and Kinnersley (2004) in the next section. The grids are constructed with hexahedral grids. The average grid size in the horizontal direction is approximately 0.006 m near the cone and two-dimensional hill, and the grid size is increased away from these areas. The vertical grid is geometrically stretched away from the boundary by clustering the grid points near the bottom surfaces where the smallest grid size is approximately 0.005 m. The total number of grids is approximately one million for the two-dimensional hill and two million for the cone. The tracer gas is released from a point source 0.0125 m from the bottom surface (the third grid point from the surface) 0.9 m upwind of the top of the ridge and 1.3 m upwind of the conical point. The tracer gases are released at a steady emission rate Q of 25 gl^{-1} from a point source, and the release is simulated by adding a source term for the tracer gas (S_q) to Eq. (3). Even though small particles with particle diameters from 0.75 μm to 1 μm were used in the wind-tunnel experiments (Parker and Kinnersley, 2004), the presented RANS treats the particles as gases due to their very small terminal velocity. As shown in Fig. 2, the inflow conditions for the velocity and turbulent kinetic energy are set based on the results of the wind-tunnel experiments by Parker and Kinnersley (2004) over a flat terrain. The convection terms in all the equations are discretized by a third-order upwind scheme, and the other terms are estimated using a second-order central scheme. The generalized logarithmic law is used on the bottom surface for the velocities and turbulent quantities, and slip boundary conditions are imposed on the velocities on the upper, lower, and outlet boundaries. Slip boundary conditions state that the velocity normal to the free-slip wall is zero and that the gradient of the velocity parallel to the wall should be zero. Neumann boundary conditions (zero-normal derivatives) are imposed on the scalar, turbulent quantities of the upper, bottom, outlet, and wall boundaries.

In this study, the reference concentration C_1 for the

dry deposition model in Eq. (10) is used as the first grid concentration above the surface and a deposition velocity of 0.003 m s^{-1} is applied. The deposition velocity is estimated by a particle diameter of nearly 1 μm, which was the size used in the wind-tunnel experiment by Parker and Kinnersley (2004).

3.2 Results

Fig. 3 shows the vertical distributions of the mean streamwise velocity over the two-dimensional hill and cone. Here x' represents the streamwise distance from the peak of the ridge or the conical point. Fig. 4 shows the streamwise distributions of the mean streamwise velocity and the root-mean squared values of the streamwise velocity fluctuation u_{rms} 0.005 m above the bottom surface. The value of u_{rms} is estimated using

$$u_{rms}=\sqrt{\frac{2}{3}k}, \tag{15}$$

where k is the turbulent kinetic energy. To quantify the comparison, the normalized mean square error (*NMSE*), fractional bias (F), and correlation coefficient (R) are computed (Santiago *et al*. 2007):

$$NMSE=\frac{\sum_{i=1}^{n}(E_i-P_i)^2}{\sum_{i=1}^{n}(E_iP_i)}, \tag{16}$$

$$FB=\frac{\bar{E}-\bar{P}}{0.5(\bar{E}+\bar{P})}, \tag{17}$$

$$R=\frac{\sum_{i=1}^{n}[(E_i-\bar{E})(P_i-\bar{P})]}{[\sum_{i=1}^{n}(E_i-\bar{E})^2]^{1/2}[\sum_{i=1}^{n}(P_i-\bar{P})^2]^{1/2}}, \tag{18}$$

where n is the number of points, E_i and P_i are the wind-

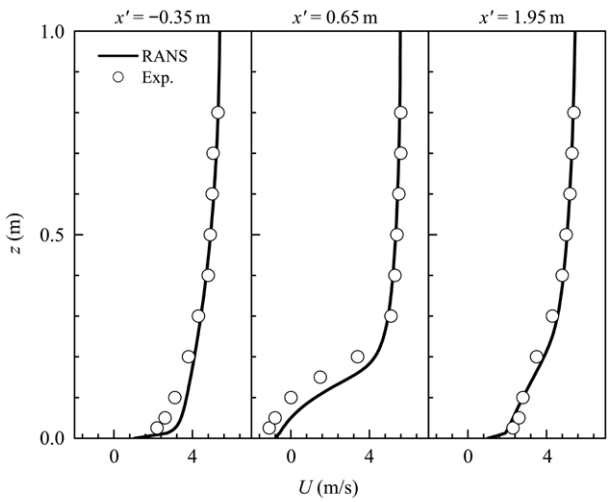

(a) Two-dimensional hill

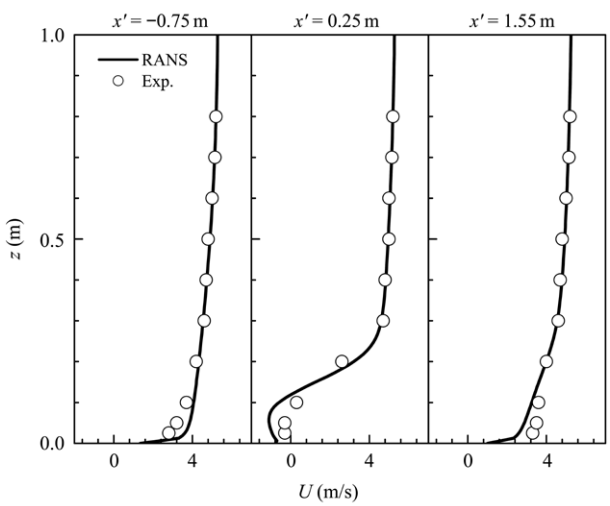

(b) Cone

Fig. 3. Vertical distributions of the streamwise velocity.

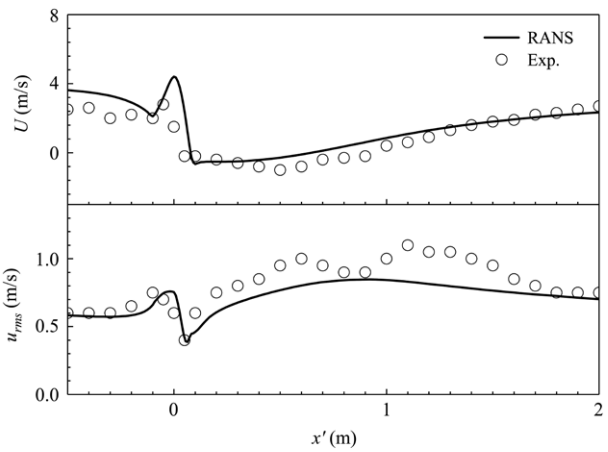

(a) Two-dimensional hill

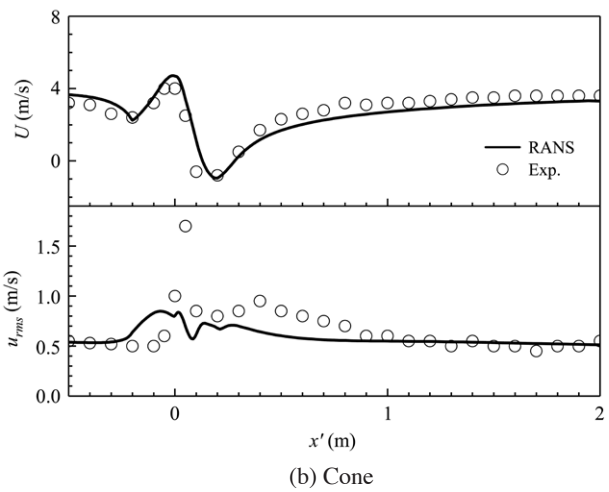

(b) Cone

Fig. 4. Streamwise distributions of the streamwise velocity and the root-mean squared values of the streamwise velocity fluctuation above the bottom surface.

Table 1. Values of *NMSE*, *FB*, and *R* for the velocity and the root-mean squared values of the streamwise velocity fluctuation.

		NMSE	*FB*	*R*
Two-dimensional hill	U	0.049	−0.132	0.980
	u_{rms}	0.031	0.128	0.860
Cone	U	0.017	0.034	0.958
	u_{rms}	0.151	0.192	0.741

tunnel experimental data and the computed values, respectively, and the overbar denotes the mean values. Table 1 shows the values of *NSME*, *FB*, and *R* for the velocity and the root-mean squared values of the streamwise velocity fluctuation. For a two-dimensional hill, the low values of *NMSE* and *FB* and the high values of *R* for the velocity indicate that the presented RANS largely represents the mean streamwise velocities. However, the negative value of *FB* indicates that the calculated velocity is substantially larger than the wind-tunnel data. As shown in Figs. 3(a) and 4(a), the calculated velocities behind the two-dimensional hill are larger than the wind-tunnel data near the ground. This overestimation was observed by the RANS of Sada *et al.* (2008), which indicated that the calculated velocities at the crest ($x' = 0$) were larger than those of the experiment in the vicinity of the ground, and this increase in the velocity affects the flow behind the hill. For the cone, low values of *NMSE* and *FB* and high values of *R* for the velocity were obtained. However, the RANS underestimates the mean streamwise velocities behind the cone, which is similar to the results of Parker and Kinnersley (2004) and Balogh *et al.* (2012). The FB for u_{rms} for both the two-dimensional hill and the cone indicates that the calculated value of u_{rms} is completely underestimated. This trend is very similar to the results of Balogh *et al.* (2012). Therefore, the presented RANS can simulate comparable profiles of the mean streamwise velocities to normal RANS predictions.

Fig. 5 shows a contour plot of the deposition rate (μg m^{-2} s^{-1}) for the two-dimensional hill and cone. Unfortunately, because there is no deposition rate for the two-dimensional hill, a direct comparison of these data with those of the experiments cannot be performed. For the two-dimensional hill, the dry deposition rate is quite high on the windward slope and rapidly decreases in the wake region behind the hill. This is because the high gas concentration at the peak of the ridge mostly disperses upward and cannot easily diffuse into the cavity region behind the hill (Sada *et al.*, 2008). Conversely, the pattern of the deposition rate for the cone is very complex. Part of the gas disperses around the cone, and an increased deposition rate is observed around the

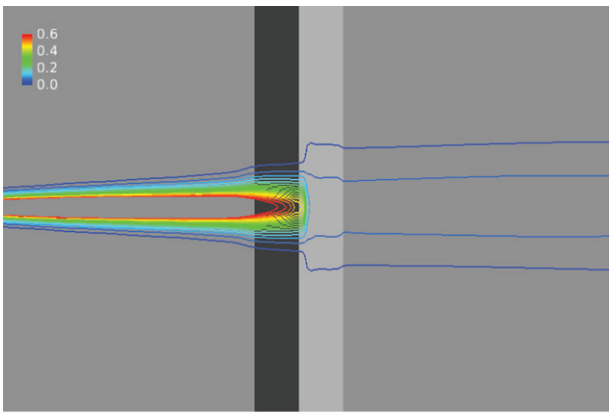

(a) Two-dimensional hill

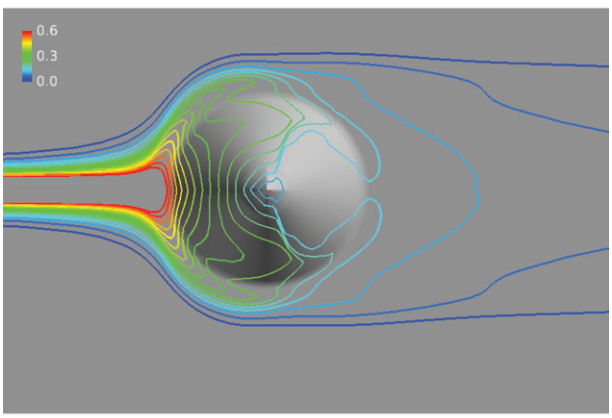

(b) Cone

Fig. 5. Distribution of the dry deposition rate (μg m^{-2} s^{-1}).

sides of the cone. This pattern and its values are very similar to those of the wind-tunnel experiments by Parker and Kinnersley (2004). However, in the presented simulation, the windward deposition rate is slightly overestimated compared to the wind-tunnel experiment. As shown in Fig. 5(b), the pattern of the deposition rate is symmetric in the presented RANS, whereas the pattern in the wind tunnel (Parker and Kinnersley, 2004) is slightly asymmetry and the ratio of the gas dispersing around the side is higher than that in the presented RANS. This difference results in an overestimation of the deposit ratio on the windward side in the presented RANS. This overestimation is also observed by the RANS of Parker and Kinnersley (2004).

4. WET DEPOSITION FOR THE MODEL TERRAIN

4. 1 Computational Conditions

Fig. 6 shows a schematic diagram of the computa-

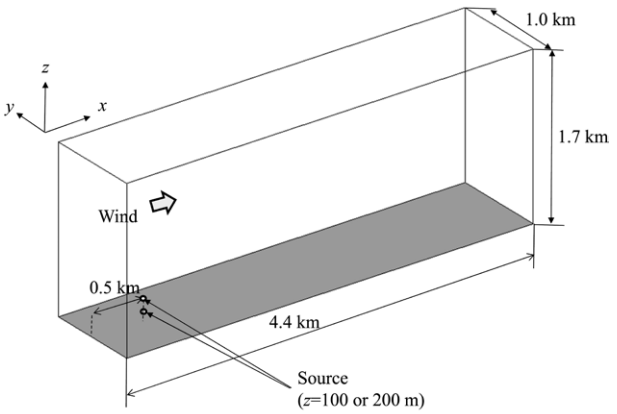

(a) Flat

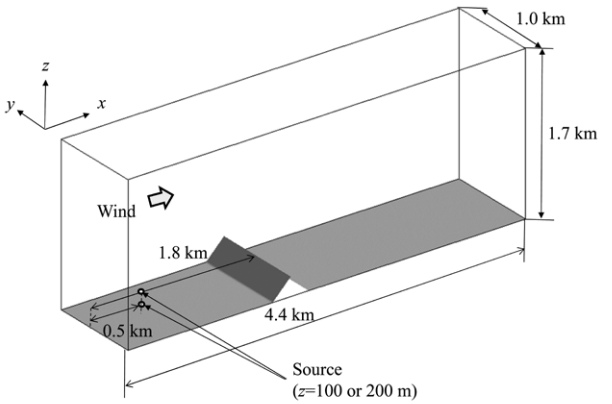

(b) Two-dimensional hill

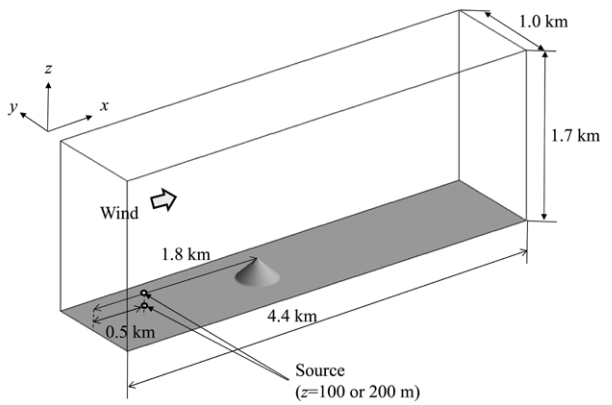

(c) Cone

Fig. 6. The computational domains for wet deposition.

tional domains for the flat terrain, two-dimensional hill, and cone. The computational conditions are shown in Table 2. The computational domains are 4.4 km × 1.0 km × 1.7 km in the $x \times y \times z$ dimensions. The origin of the coordinate axis is the central lower surface of

Table 2. Computational conditions.

Case	Terrain	Source height (m)	W (m/s)
F0-P	Flat	0	(0, 0, −4.52)
F1-P	Flat	100	(0, 0, −4.52)
F1-M	Flat	100	(0, 0, −45.2)
F2-P	Flat	200	(0, 0, −4.52)
F2-M	Flat	200	(0, 0, −45.2)
2D0-P	2D	0	(0, 0, −4.52)
2D1-P	2D	100	(0, 0, −4.52)
2D1-M	2D	100	(0, 0, −45.2)
2D2-P	2D	200	(0, 0, −4.52)
2D2-M	2D	200	(0, 0, −45.2)
3D0-P	Cone (3D)	0	(0, 0, −4.52)
3D1-P	Cone (3D)	100	(0, 0, −4.52)
3D1-M	Cone (3D)	100	(0, 0, −45.2)
3D2-P	Cone (3D)	200	(0, 0, −4.52)
3D2-M	Cone (3D)	200	(0, 0, −45.2)

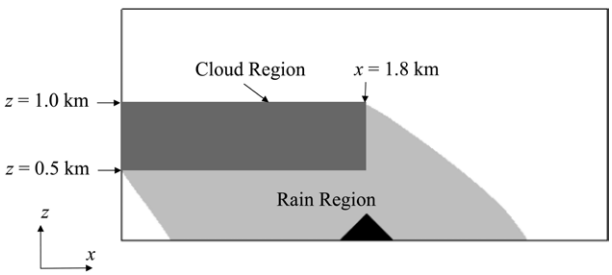

Fig. 7. Images of the cloud and rain regions.

the entrance in the computational domain. The three-dimensional terrain is conical in shape with a height of 200 m and a slope of 45°. The conical point is located 1.8 km downwind of the entrance. The other terrain is a two-dimensional hill with a height of 200 m and a lateral width of 1000 m, which is equal to the lateral length of the computational domain. The top of the ridge is located 1.8 km downwind of the entrance of the computational domain. Even though the distance between the source point and the top of the ridge (conical point) is different in Section 3, the same distance of 1.3 km is used in this simulation in order to compare their results. The three different source heights are 0 m, 100 m, and 200 m. The inflow conditions for the velocity and turbulent kinetic energy are set based on the profile in Fig. 2 scaled up 1000 times. The boundary layer height z is 800 m and the free velocity at this height is 4.8 m s^{-1}.

The cloud region is defined from the entrance of the computational domain to the crest of the two-dimensional hill or cone (0 km $\leq x \leq$ 1.8 km and 0.5 km $\leq z \leq$ 1.0 km), as shown in Fig. 7. If the governing equation of the rainwater is not solved and the rainwater falls

with the force of gravity under this cloud region, the wet deposition rate behind the hill or cone is completely zero. Because the rainwater is advected by wind and dispersed by turbulence using Eq. (14) in this simulation, the rain region spreads downwind, as shown in Fig. 7.

The scavenging coefficient in Eq. (11) is expressed as

$$\Lambda = \alpha \gamma^{\beta}, \tag{19}$$

where α and β are parameters determined for each chemical species and γ (mm h^{-1}) is the precipitation intensity. In this simulation, a heavy rain is assumed with $\gamma = 10$ mm h^{-1} to examine the model performance for wet deposition [$\alpha = 5.0 \times 10^{-5}$ and $\beta = 0.8$ (Terada *et al.*, 2004)]. The terminal velocity of the rain, $W = (0, 0, -4.52)$ is estimated using

$$W = (0, 0, -3100 d_d), \tag{20}$$

where

$$d_d = 9.0 \times 10^{-4} \gamma^{0.21}, \tag{21}$$

(Seinfeld and Pandis, 2006). In frequently used mesoscale numerical models coupled with atmospheric chemistry, the scalar scavenged by raindrops deposits directly to the Earth's surface without advection and dispersion. In this simulation, the above phenomena are not simulated because the scalar scavenged by raindrops is solved using Eq. (13). As an alternative procedure, a ten times higher terminal velocity for the rain is used only in Eq. (13). Because this procedure makes the scalar scavenged by raindrops fall to the Earth's surface quickly and is similar to the behavior of the frequently used wet deposition model, it is called the "normal wet deposition model" in this paper.

4.2 Results

To investigate the performance of the proposed wet deposition model using the cases of a tracer gas released at $z = 100$ m or 200 m, Fig. 8 shows the streamwise distributions of the wet deposition rate for the flat terrain, two-dimensional hill, and cone at $y = 0$. The wet deposition rate W_g is normalized by the source strength Q. Note that dry deposition is disregarded because gases released from a relatively high point scarcely disperse near the ground. In the flat terrain cases using the normal wet deposition model (Cases F1-M and F2-M), the peak of the wet deposition rate is observed near the source location at $x' = -1.3$ km because the scalar released from the sources at $z = 100$ m or 200 m is immediately scavenged by raindrops and deposited to the surface directly below the source. Conversely, in the proposed wet deposition model (Cases F1-P and F2-P), the scalar scavenged by rain near the source disperses downwind and the scalar reaching the surface deposits downwind of the source. This trend is apparent as the source height increases. In addition, a difference in the wet deposition rate is also observed near the downwind edge of the rain region for $x' > 1.0$ km due to the same behavior near the source. However, except for the source neighborhood and the downwind edge of the rain region, both wet deposition rates are very similar over the flat region.

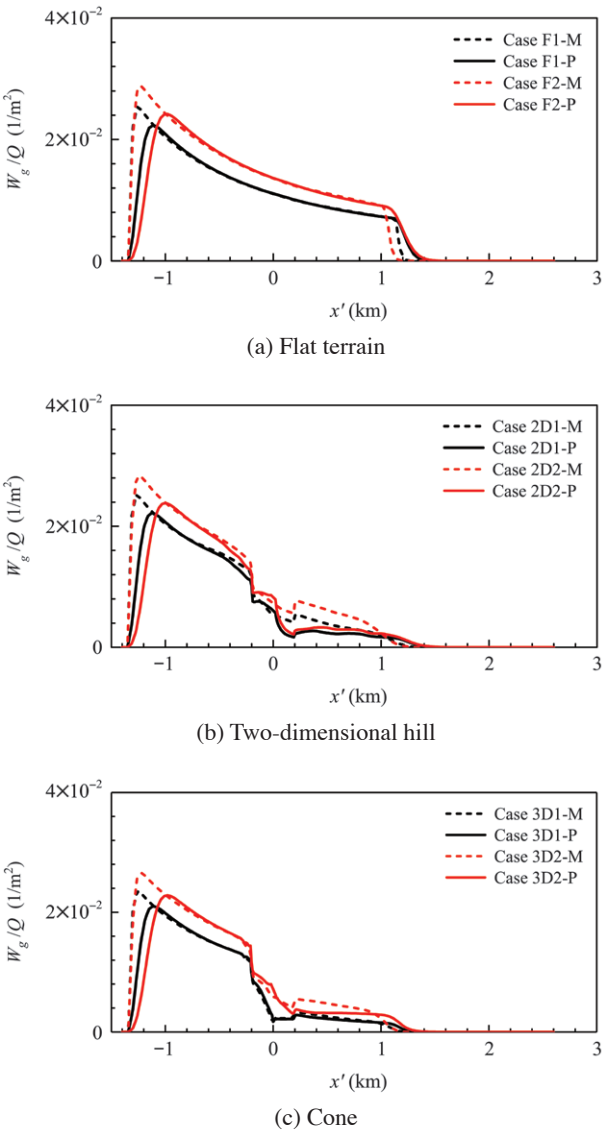

Fig. 8. Streamwise distribution of the wet deposition rate.

As for the two-dimensional hill, the behavior of the wet deposition rate is very similar to the flat case near the source; however, the wet deposition rate near the two-dimensional hill decreases in all cases compared to that for the flat surface shown in Fig. 8(a) because the terrain enhances the scalar dispersion and the area

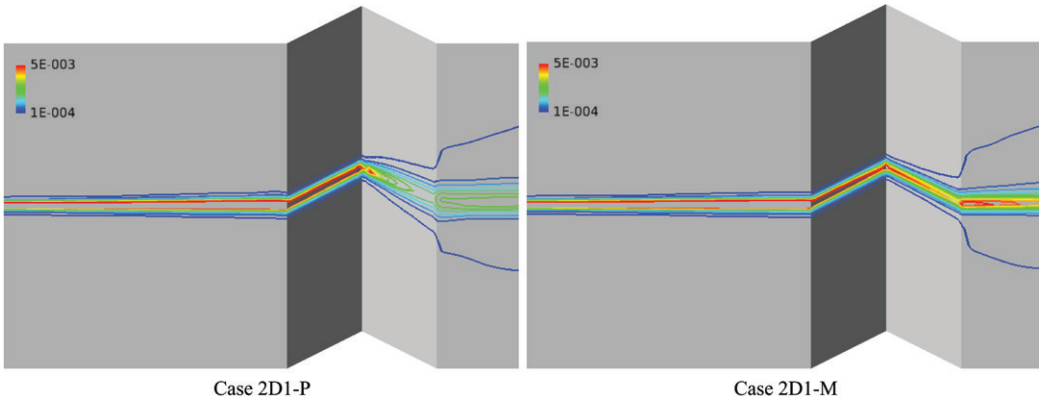

(a) Two-dimensional hill

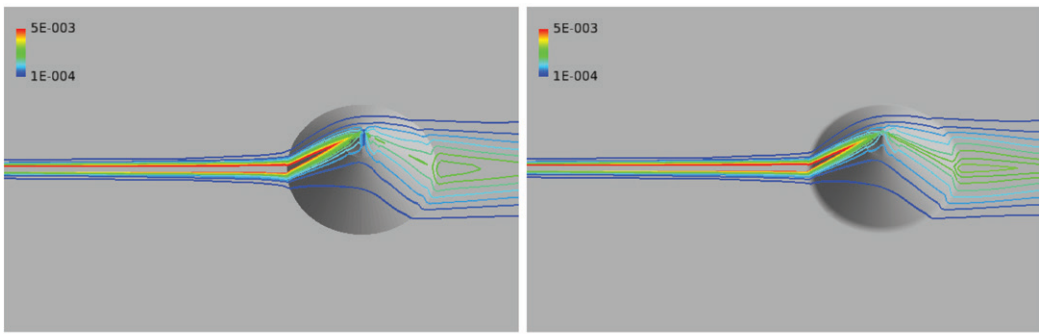

(b) Cone

Fig. 9. Contour plot of the wet deposition rate (the wet deposition rate is normalized by the source strength).

at the ground surface increases owing to the slope inclination. Downwind of the ridge, the wet deposition rate in the proposed model (Cases 2D1-P and 2D2-P) is lower than that in the normal deposition model (Cases 2D1-M and 2D2-M). In Case 2D1-M, the scalar scavenged by raindrops and deposited to the surface is less affected by turbulence and a highly narrow wet deposition rate at the ground is observed downwind of the ridge, as shown in Fig. 9(a). In Case 2D1-P, the high level of turbulence generated behind the two-dimensional hill disperses the scalar scavenged by raindrops in the horizontal direction and the wet deposition at the ground is widely distributed. As the source height increases, the difference in the wet deposition rate becomes larger because the advection distance of the scalar becomes longer.

As for the cone, the behavior of the wet deposition rate is also very similar to the flat case near the source and the wet deposition rate is dramatically decreased compared to both the flat and two-dimensional cases. Part of the scalar windward of the cone disperses over the cone, while the other part disperses to both sides of the cone, indicating that the scalar concentration becomes smaller due to the terrain. Behind the cone, the wet deposition rate using the proposed model (Cases 3D1-P and 3D2-P) is slightly smaller than that using the normal deposition model (Cases 3D1-M and 3D2-M) for exactly the same reason as in the case of the two-dimensional hill.

Fig. 10 shows the wet deposition ratio relative to the flat terrain for the two-dimensional hill and the cone using the proposed deposition model. The wet deposition ratio near the source is mostly unity; however, the wet deposition ratio in both cases becomes smaller after the windward edge of the hill or cone and finally reaches approximately a quarter of the wet deposition ratio. Therefore, the terrain acts to disperse the scalar and decrease the peak wet deposition rate downwind of the terrain when the source height is relatively high.

To investigate the effect of the terrain on the dry and wet deposition under a lower source height, the dry and wet deposition ratio of the ground level source over the flat terrain, two-dimensional hill, and cone is shown in Fig. 11 The dry deposition rate F_g and the

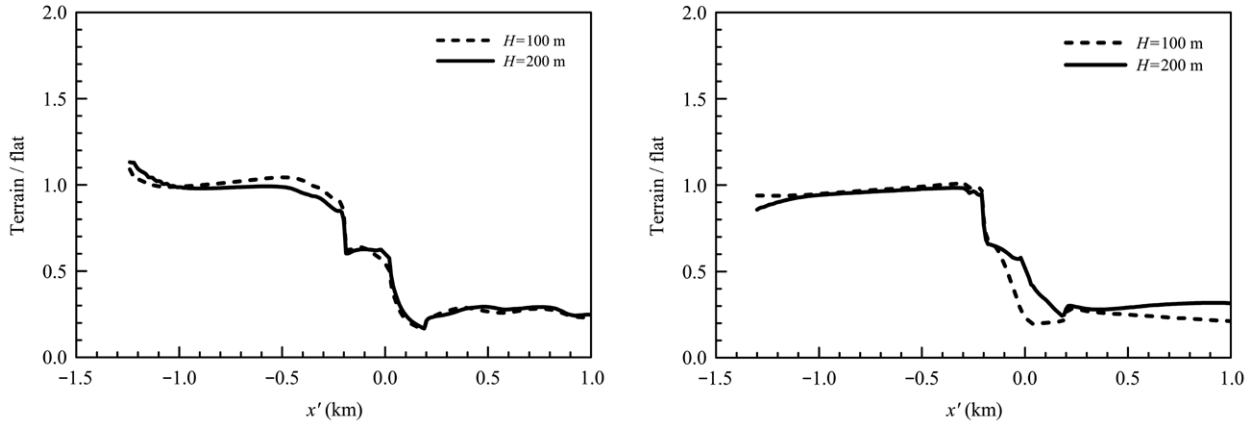

(a) Two-dimensional hill (b) Cone

Fig. 10. Deposition ratio relative to flat terrain.

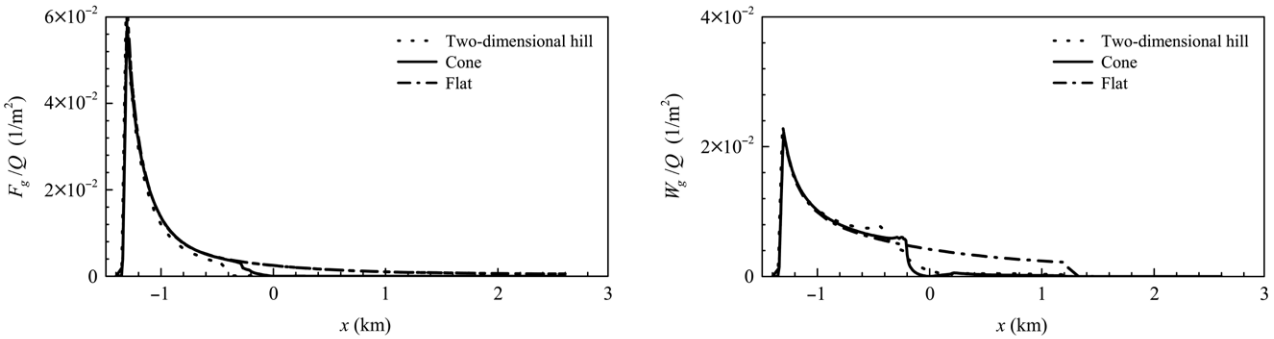

(a) Dry deposition rate (b) Wet deposition rate

Fig. 11. Streamwise distribution over the flat terrain, two-dimensional hill, and cone.

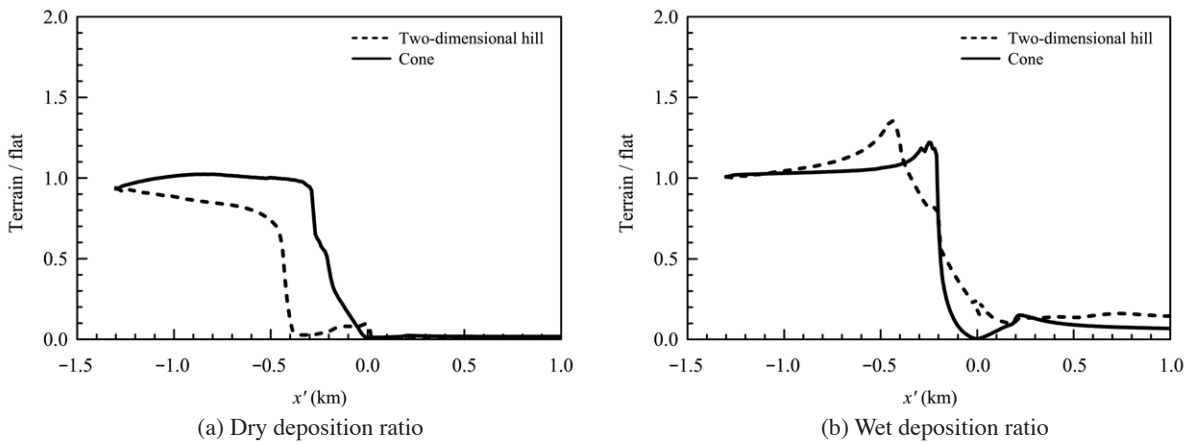

(a) Dry deposition ratio (b) Wet deposition ratio

Fig. 12. Deposition ratio relative to flat terrain.

wet deposition rate W_g are normalized by the source strength Q. Fig. 12 shows the deposition ratio for the dry and wet deposition relative to the flat terrain. A high dry deposition rate in all cases (Cases F0-P, 2D0-P, and 3D0-P) is observed near the source in Fig. 11, and the rate dramatically decreases in the downwind

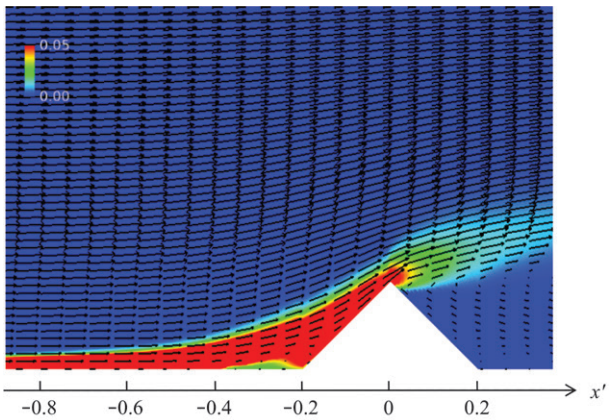

(a) Two-dimensional hill

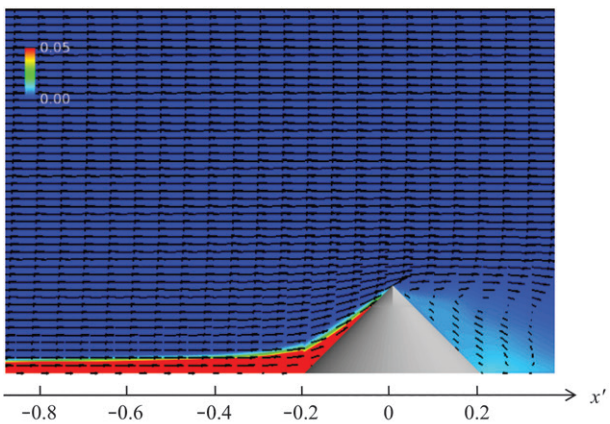

(b) Cone

Fig. 13. Contour plot of the tracer gas concentration and velocity vector (the concentration is normalized by the initial value).

distance in an exponential manner. A steep decrease in the dry deposition ratio on the flat terrain is observed at $x' = -0.4$ km for the two-dimensional hill and at $x' = -0.2$ km for the cone. The position for the cone corresponds to its windward edge, which indicates that the cone affects the dry deposition. For the two-dimensional hill, because an upward flow is generated at $x' = -0.4$ km, as shown in Fig. 13, and accompanies the scalar upward, a steep decrease is observed at $x' = -0.4$ km.

A high wet deposition rate in both cases is observed near the source in Fig. 11(b), and the wet deposition rate relative to the flat surface near the terrain dramatically decreases because the terrain enhances the gas dispersion. However, a wet deposition ratio of more than unity is observed on the windward side of the terrain, as shown in Fig. 12(b). This is attributed to the fact that the streamwise velocity is decelerated by the windward terrain and this deceleration tends to increase the wet deposition. This indicates that the wet deposition is occasionally increased by the terrain under a lower source height.

5. CONCLUSION

The applicability of the dry and wet deposition models to high-resolution numerical simulations was investigated to estimate the deposition using CFD models with high grid resolutions. First, to confirm the applicability of the frequently used formulation for dry deposition to a high-resolution CFD model, a RANS simulation was implemented for a cone and a two-dimensional ridge. The results were compared to wind-tunnel experiments (Parker and Kinnersley, 2004). The results show that the dry deposition rate mostly corresponds to that in the wind-tunnel experiments. This confirms the possible application of the dry deposition model to high-resolution simulations.

Second, to predict the wet deposition rate at an exact position, the transport equation of a new scalar concentration scavenged by rain droplets was developed for the wet deposition model. A sensitivity analysis of the proposed wet deposition procedure was implemented. In the frequently used wet deposition model, the scalar scavenged by raindrops deposits to the surface directly below the scavenging point and a highly narrow wet deposition rate at the ground is observed downwind of the ridge. Conversely, with the proposed procedure, the high level of turbulence generated behind the ridge disperses the scalar scavenged by raindrops in the horizontal direction and the wet deposition at the ground is widely distributed. Therefore, the proposed wet deposition procedure considering the dispersion of scalars scavenged by raindrops shows a different distribution of the wet deposition rate from that of the frequently used model. These results indicate an accuracy improvement for the wet deposition rate in RANS with a high-resolution grid considering the effect of different terrains on wet deposition. Because there are no reliable experimental data for the wet deposition rate for a cone or a two-dimensional ridge, the accuracy of the proposed procedure has not yet been confirmed. To construct a reliable model, a comparison of the wet deposition obtained by the proposed wet deposition model with observations is required.

The proposed procedure contributes to accuracy improvements for the deposition rate in a high-resolution simulation; however, additional validation case studies (e.g., grid sensitivity and real terrain) are needed to improve the accuracy of the proposed procedure.

ACKNOWLEDGEMENT

This research was partially supported by the Japan Society for the Promotion of Science (JSPS), KAKENHI (15K06343).

REFERENCES

Balogh, M., Parente, A., Benocci, C. (2012) RANS simulation of ABL flow over complex terrains applying an Enhanced κ-ε model and wall function formulation: Implementation and comparison for fluent and OpenFOAM. Journal of Wind Engineering and Industrial Aerodynamics 104-106, 360-368.

Franke, J., Hellsten, A., Schlünzen, H., Carissimo, B. (2007) Best practice guideline for the CFD simulation of flows in the urban environment. COST Action 732, 52.

Hendricks, E.A., Diehl, S.R., Burrows, D.A., Keith, R. (2007) Evaluation of a fast-running urban dispersion modeling system using joint urban 2003 field data. Journal of Applied Meteorology and Climatology 46, 2165-2179.

Jänhall, S. (2015) Review on urban vegetation and particle air pollution – Deposition and dispersion. Atmospheric Environment 105, 130-137.

Kajino, M., Inomata, Y., Sato, K., Ueda, H., Han, Z., An, J., Katata, G., Deushi, M., Maki, T., Oshima, N., Kurokawa, J., Ohara, T., Takami, A., Hatakeyama, S. (2012) Development of the RAQM2 aerosol chemical transport model and predictions of the Northeast Asian aerosolo mass, size, chemistry, and mixing type. Atmospheric Chemistry and Physics 12, 11833-11856.

Katata, G., Ota, M, Terada, H., Chino, M., Nagai, H. (2012a) Atmospheric discharge and dispersion of radionuclides during the Fukushima Dai-ichi Nuclear Power Plant accident. Part I: Source term estimation and local-scale atmospheric dispersion in early phase of the accident. Journal of Environmental Radioactivity 109, 103-113.

Katata, G., Terada, H., Nagai, H., Chino, M. (2012b) Numerical reconstruction of high dose rate zones due to the Fukushima Dai-ichi Nuclear Power Plant accident. Journal of Environmental Radioactivity 111, 2-12.

Kondo, H., Asahi, K., Tomizuka, T., Suzuki, M. (2006) Numerical analysis of diffusion around a suspended expressway by a multi-scale CFD model. Atmospheric Environment 40, 2852-2859.

Kurose, R., Anami, M., Fujita, A., Komori, S. (2012) Numerical simulation of flow pass a heated/cooled sphere. Journal of Fluid Mechanics 692, 332-346.

Lin, Y.-L., Farley, R.D., Orville, H.D. (1983) Bulk parameterization of the snow field in a cloud model. Journal of Applied Meteorology 22, 1065-1092.

Michioka, T., Chow, F.K. (2008) High-resolution large-eddy simulations of scalar transport in atmospheric boundary flow over complex terrain. Journal of Applied Meteorology and Climatology 47, 3150-3169.

Michioka, T., Sato, A., Sada, K. (2013) Large-eddy simulation coupled to mesoscale meteorological model for gas dispersion in an urban district. Atmospheric Environment 75, 153-162.

Morino, Y., Nagashima, T., Sugata, S., Sato, K., Tanabe, K., Noguchi, T., Takami, A., Tanimoto, H., Ohara, T. (2015) Verification of chemical transport models for $PM_{2.5}$ chemical composition using simultaneous measurement data over Japan. Aerosol and Air Qualuty Research 15, 2009-2023.

Nakayama, H., Takemi, T., Nagai, H. (2015) Large-eddy simulation of turbulent winds during the Fukusima Daiichi nuclear power plant accident by coupling with a meso-scale meteorological simulation model. Advances in Science and Research 12, 127-133.

Parker, S.T., Kinnersley, R.P. (2004) A computational and wind tunnel study of particle dry deposition in complex topography. Atmospheric Environment 38, 3867-3878.

Pesava, P., Aksu, R., Toprak, S., Horvath, H., Seidl, S. (1999) Dry deposition of particles to building surfaces and soiling. Science of The Total Environment 235, 25-35.

Sada, K., Michioka, T., Ichikawa, Y. (2008) Numerical model for stack gas diffusion in terrain containing buildings – Application of numerical model to a cubical building and a ridge terrain. Asian Journal of Atmospheric Environment 2-1, 1-13.

Santiago, J.L., Martilli, A., Martin, F. (2007) CFD simulation of airflow over a regular array of cubes. Part I: Three-dimensional simulation of the flow and validation with wind-tunnel measurements. Boundary-Layer Meteorology 122, 609-634.

Seinfeld, J.H., Pandis, S.N. (2006) Atmospheric chemistry and physics: From air pollution to climate change, Second Edition, Wiley, 1203.

Sekiyama, T.T., Kuni, M., Kajino, M., Shimbori, T. (2015) Horizontal resolution dependence of atmospheric simulations of the Fukushima nuclear accident using 15-km, 3-km, and 500-m grid models. Journal of the meteorological society of Japan 93, 49-64.

Slinn, S.A., Slinn, W.G.N. (1980). Predictions for particle deposition on natural waters. Atmospheric Environment 24, 1013-1016.

Terada, H., Chino, M. (2008) Development of an atmospheric dispersion model for accidental discharge of radionuclides with the function of simultaneous prediction for multiple domains and its evaluation by application to the Chernobyl nuclear accident. Journal of Nuclear Science and Technology 45, 920-931.

Terada, H., Furuno, A., Chino, M. (2004) Improvement of worldwide version of system for prediction of environmental emergency dose information (WSPEEDI), (I) New combination of models, atmospheric dynamic model MM5 and particle random walk model GEARN-new. Journal of Nuclear Science and Technology 41,

632-640.
Tominaga, Y., Stathopoulos, T. (2007) Turbulent Schmidt numbers for CFD analysis with various types of flow field. Atmospheric Environment 41, 8091-8099.
Wesely, M.L. (1989) Parameterization of surface resistances to gaseous dry deposition in regional-scale numerical models. Atmospheric Environment 23, 1293-1340.

(Received 7 June 2017, revised 23 August 2017, accepted 23 August 2017)